THE ASTROPHYSICAL JOURNAL, 439:771–778, 1995 February 1


# SPATIALLY RESOLVED SUBMILLIMETER CONTINUUM EMISSION TOWARD L1551 IRS 5

E. F. LADD[1]
Institute for Astronomy, University of Hawaii, 2680 Woodlawn Drive, Honolulu, HI 96822;
ladd@fcrao1.phast.umass.edu

G. A. FULLER[2]
National Radio Astronomy Observatory,[3] 949 North Cherry Avenue, Campus Building 65, Tucson, AZ 85721

R. PADMAN
Mullard Radio Astronomy Observatory, Cavendish Laboratory, Madingley Road, Cambridge, England CB3 0HE

P. C. MYERS
Harvard-Smithsonian Center for Astrophysics, Mail Stop 42, 60 Garden Street, Cambridge, MA 02138

AND

FRED C. ADAMS
Physics Department, University of Michigan, Ann Arbor, MI 48109
*Received 1994 May 9; accepted 1994 August 3*

## ABSTRACT

We present high signal-to-noise ratio 16″–20″ resolution submillimeter continuum images of the embedded young stellar object L1551 IRS 5. The images are dominated by a compact source at the position of IRS 5, which has a deconvolved size of 10″ ± 3″. Low-level emission extends up to 5000 A.U. from IRS 5 and is distributed nonaxisymetrically. The 1100 $\mu$m emission is extended in the north-south direction and is elliptical in shape. In contrast, our 730 $\mu$m map shows emission in a cross-shaped pattern, with arms extending to the north, south, east, and west of IRS 5. The cross emission is not an artifact of our observational methods but rather is intrinsic to the source distribution. We model the submillimeter continuum emission at 1100 $\mu$m and 730 $\mu$m using three components: an unresolved point source; a cold ($\sim$12 K), massive ($\sim$1 $M_\odot$), smoothly distributed envelope; and a warm ($\gtrsim$50 K), less massive ($\lesssim$0.02 $M_\odot$) "cross" centered at the position of IRS 5. We note that the arms of the cross are well aligned with the edges of the CO outflow from IRS 5 and suggest that they may consist of core material warmed and pushed aside by the energetically dominant outflow.

*Subject headings:* infrared: ISM: continuum — ISM: individual (L1551 IRS 5) — ISM: jets and outflows — stars: pre–main-sequence

## 1. INTRODUCTION

The distribution of material around a forming star is undoubtedly influenced by the same dynamic processes which contribute to the formation of the star itself. While on the largest scales (i.e., 0.1–1.0 pc), the dense cores out of which stars form have aspect ratios of about 2 (Benson & Myers 1989; Myers et al. 1991), the very small scale ($\lesssim$100 A.U.) structure is inferred to be extremely anisotropic, most probably in the form of a circumstellar disk (Strom et al. 1985; Campbell et al. 1987; Hodapp et al. 1988; Sargent et al. 1988). The cause of this increase in anisotropy from large to small scale is not clearly understood, although it is likely that core rotation and collimated bipolar outflows play an important role in the process (i.e., conservation of angular momentum).

In this paper and a companion work (Fuller et al. 1994), we examine the distribution of material on $\sim$3000 A.U. size scales around L1551 IRS 5 using low optical depth tracers of circumstellar gas and dust. The submillimeter continuum is particularly well suited to a study of the circumstellar dust distribution because of (1) the low optical depth at these wavelengths even toward deeply embedded sources, (2) the small beam size now available with large submillimeter telescopes, and (3) the sensitivity to even the coolest dust in the region.

L1551 IRS 5 (Strom, Strom, & Vrba 1976) has the advantages of being nearby (140 pc; Elias 1978), relatively luminous ($\sim$30 $L_\odot$; Cohen et al. 1984), and deeply embedded. It has been the source of intensive study at wavelengths ranging from the optical through the infrared and into the radio, and has been classified as a Class I object in the spectral energy distribution classification scheme of Adams, Lada, & Shu (1987), indicating that it is a deeply embedded protostar still accreting material from its placental core. L1551 IRS 5 also drives a bipolar outflow, and thus it is likely that infall and outflow are taking place simultaneously in this object. It has been observed in the millimeter continuum with single-dish telescopes by Keene & Masson (1988) and Walker, Adams, & Lada (1990). In both investigations, an envelope around the source was found to be extended on $\sim$20″ scales. Keene & Masson (1988) observed this source with an interferometer, and found a small (45 A.U.) millimeter continuum source centered at the position of IRS 5. Recently, Lay et al. (1994) have observed this source at 850 $\mu$m with an interferometer and found a similarly sized continuum source.

This paper is organized as follows. We present high signal-to-noise ratio images of IRS 5 at 1100 $\mu$m, 850 $\mu$m, and 730 $\mu$m

[1] Current Address: Five College Radio Astronomy Observatory, Lederle Graduate Research Center, University of Massachusetts, Amherst, MA 01003.
[2] Current address: NRAO, 520 Edgemont Road, Charlottesville, VA 22903.
[3] NRAO is operated by Associated Universities, Inc., under cooperative agreement with the National Science Foundation.

in § 2. We analyze the spatial distribution of emission and the spectral properties in § 3. We present a simple model for the submillimeter emission and discuss the interaction between the dense core around IRS 5 and the bipolar outflow emanating from the embedded source in § 4. We present our conclusions in § 5.

## 2. OBSERVATIONS

Submillimeter observations were made with the 15 m James Clerk Maxwell Telescope[4] (JCMT) in 1991 October. The continuum maps were obtained using the facility UKT-14 bolometer system and the standard broadband submillimeter filter set with passbands centered at approximately 1100 $\mu$m, 850 $\mu$m, and 730 $\mu$m. We chopped in azimuth with a frequency of approximately 8 Hz and a chopper throw of 60″. We raster scanned in the chop direction at a rate of 5″ $s^{-1}$ and binned the data in 1 s intervals, creating 5″ pixels in azimuth and elevation. From this chopped, raster-scanned dataset, we reconstructed maps using both the NOD2 system (Haslam 1974) as modified for use at the JCMT, and (for the 730 $\mu$m maps only) the maximum entropy deconvolution program DBMEM (Richer 1992). The resulting maps have fields of view of approximately 2′ × 2′. Calibration was provided by frequent observations of Uranus, Neptune, Jupiter, and Mars, as well as CRL 2688 and CRL 618. Several maps of Uranus (radius = 1.″9) and Mars (radius = 1.″8) were used to determine the full width at half-maximum (FWHM) size of the main beam at all three wavelengths. All maps were obtained using diffraction-limited apertures, which produced beam sizes of 19.″5 ± 0.″6, 16″ ± 1.″5, and 16″ ± 1.″5 at 1100 $\mu$m, 850 $\mu$m, and 730 $\mu$m, respectively, as measured from our beam maps of Uranus and Mars.

### 2.1. *NOD2 Restoration*

The source maps were corrected for atmospheric attenuation and scaled such that the peak value in each map was unity. The maps were converted to equatorial coordinates and co-added, and then renormalized to the flux values determined from pointed, on-off measurements of L1551 IRS 5. The beam maps were also corrected for atmospheric attenuation and scaled such that the peak value in each map was unity. They were then co-added in the azimuth-elevation (AZ-EL) frame to produce a high signal-to-noise ratio estimate of the AZ-EL beam.

In order to deconvolve the telescope beam from the source maps, we constructed an "equivalent beam map" from our AZ-EL beam maps. For each individual source map, a copy of the beam map was converted to equatorial coordinates assuming that the beam map had been made at the same azimuth and elevation as the source map. These beam maps were then averaged to produce an equivalent beam map at each wavelength which represents the effective telescope beam used to make the source maps. The equivalent beam maps were used to correct the source maps for the telescope beam.

We applied a method similar to the CLEAN algorithm (Hogböm 1974) often used on aperture synthesis data. We decomposed the observed images into point source components, using the equivalent beam maps as point source functions. CLEAN maps were constructed by convolving the point source components with Gaussian beams with FWHM equal to the measured beam FWHM size at each wavelength.

### 2.2. *DBMEM Processing*

As a check on the restoration procedure, we also applied the DBMEM deconvolution procedure (Richer 1992) to the 730 $\mu$m data. DBMEM uses the MEMSYS3 (Gull & Skilling 1989) maximum entropy kernel to estimate the true sky distribution, given the observed dual-beam, AZ-EL data and an estimate of the beam. It can thus be thought of as a constrained global-fitting procedure.

The procedure was applied in two stages. In the first, DBMEM was used to estimate the effective AZ-EL beam from our high signal-to-noise ratio observations of Uranus. The resulting beam was then used as an input to the second stage, which produced an estimate of the source distribution on a regular 2″ equatorial grid. This particular version of MEM does not assume any intrinsic correlation between nearby pixels and produces high-frequency structure for which there is little evidence in the data. The greatly oversampled output distribution was thus filtered with a Gaussian. The resulting smoothed restoration is thus produced by a processing route completely independent from the NOD2/CLEAN procedure.

## 3. RESULTS

The beam maps, NOD2 source maps, and CLEANed source maps at all three wavelengths are shown in Figure 1. The three beam maps show little azimuthal structure, with departures from circularity only at levels less than 10% of peak. Consequently, the source maps and CLEANed maps appear quite similar. The results of the DBMEM deconvolution of the 730 $\mu$m data are shown in Figure 2, first convolved with a 16″ FWHM Gaussian beam to compare directly with the results in Figure 1, and then convolved with a 10″ beam which suppresses less of the small-scale structure.

### 3.1. *Spatial Structure*

At all three wavelengths, the maps show L1551 IRS 5 is composed of a central compact component surrounded by extended emission. We estimate the size of the compact component based on cuts through the source at position angles of 45° and 135° east of north, which were chosen to minimize the contribution from the larger scale extended emission. We fit the emission within 15″ of the peak along each of these cuts with a Gaussian and find that in all three maps, the compact source has a slightly larger FWHM size than the beam. Gaussian deconvolution of the beam from the compact source profile yields a compact source size of 10″ ± 3″ (~1400 A.U.; see Table 1) in all three bands. The compact source is similar in size to the 100 $\mu$m source observed by Butner et al. (1991; ~1700 A.U.), and the flattened $C^{18}O$ structure seen by Sargent et al. (1988; ~1500 A.U.). However, it is larger than the 1.3 mm and 2.7 mm continuum source measured by Keene & Masson (1988; ~45 A.U.) and the 850 $\mu$m source measured by Lay et al (1994; 60 A.U.). We estimate the flux from the compact source by integrating a Gaussian whose size is equal to the measured size and whose peak is equal to the peak flux in each map. The size of the compact source and its fluxes are listed in Table 1, along with the peak and integrated map fluxes.

Extended emission is detected to radii of approximately 40″, 30″, and 30″ at 1100 $\mu$m, 850 $\mu$m, and 730 $\mu$m, respectively, or over a linear size of ~5000 A.U. The extended emission has

[4] The James Clerk Maxwell Telescope is operated by the Royal Observatory Edinburgh on behalf of the Science and Engineering Research Council of the United Kingdom, the Netherlands Organization for Scientific Research, and the National Research Council of Canada.

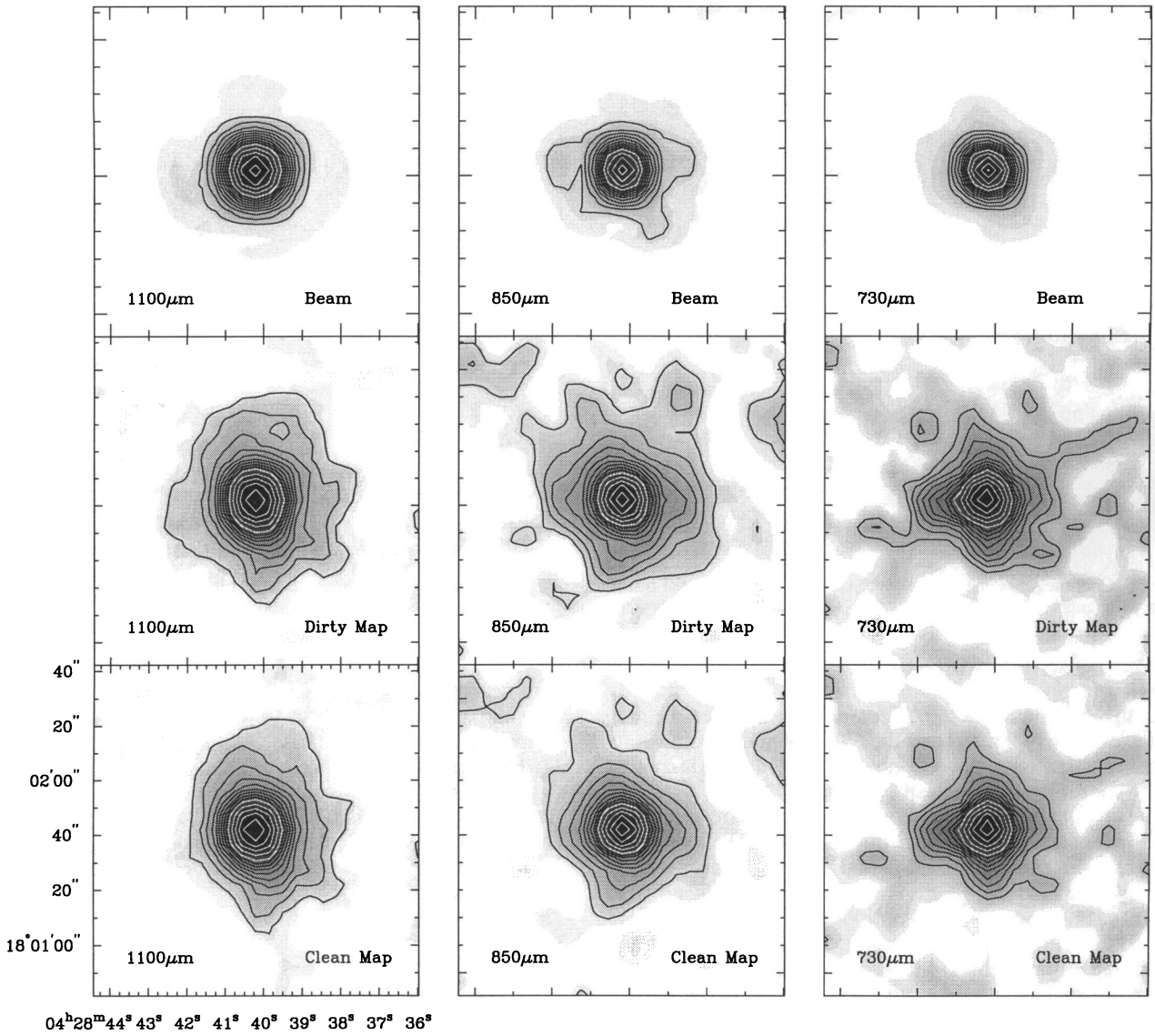


FIG. 1.—Contour maps of beam, dirty map, and clean map at 1100 μm, 850 μm, and 730 μm. Contours run from 5% to 45% of peak flux by 5% (*black*) and 50% to 90% by 10% (*white*). The 5% contour is not shown for the 730 μm maps.

azimuthal structure at all three wavelengths. At 1100 μm, the emission is roughly elliptical with a major axis in the north-south direction. At 850 μm, the north-south structure is less extended; however, there is also an extension to the east and west, which is not as prominent in the 1100 μm data. The extended emission at 730 μm is clearly resolved into a cross pattern, with arms extending to the north, south, east, and west. The cross emission is quite prominent in the "super-resolved" DBMEM map convolved with the 10″ beam, but is also clearly visible in the map convolved with the 16″ beam (Fig. 2).

We do not believe that the cross emission seen at 850 μm and 730 μm is an observational artifact, for the following reasons:

1. We see no similar cross-shaped structure in any of our beam maps, which have a larger dynamic range than the L1551 IRS 5 observations. Therefore, we conclude that the cross has

TABLE 1

OBSERVATIONAL DATA

| λ (μm) | Beam Size | Map rms (Jy beam$^{-1}$) | Peak Flux (Jy beam$^{-1}$) | Integrated Flux (Jy) | Compact Source Size | Compact Source Flux (Jy) |
|---|---|---|---|---|---|---|
| 1100..... | 19.″5 ± 0.″6 | 0.06 | 2.7 | 5.1 | 9″ ± 3″ | 3.2 |
| 850..... | 16 ± 1.5 | 0.11 | 5.4 | 16.9 | 10 ± 4 | 8 |
| 730..... | 16 ± 1.5 | 0.35 | 8.4 | 37 | 10 ± 4 | 12 |

NOTE.—The deconvolved sizes and integrated fluxes for the compact source are estimated assuming Gaussian distributions for both source and beam.

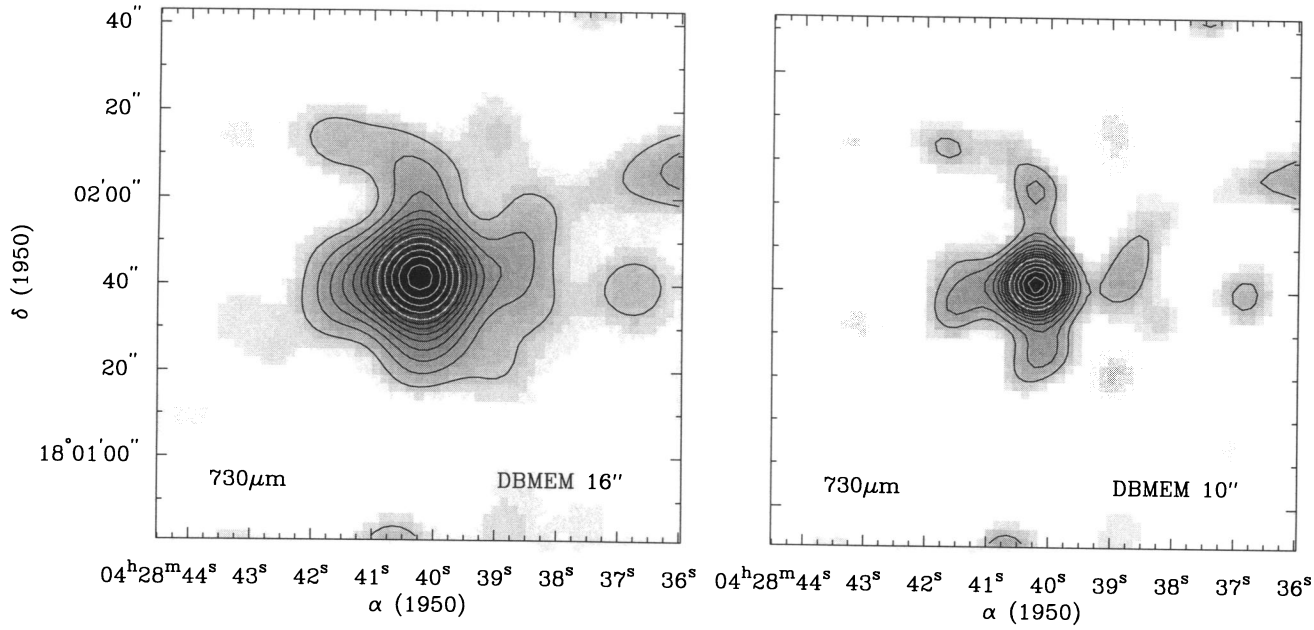


FIG. 2.—Contour maps of DBMEM reconstructions of the spatial distribution of 730 μm emission. The fitted model has been convolved with a 16″ FWHM Gaussian (*left*) and a 10″ FWHM Gaussian (*right*). Contours run from 10% to 45% of peak flux by 5% (*black*) and 50% to 90% by 10% (*white*).

not been generated by azimuthal structure in the telescope's point source response function. The similarity between the raw, uncorrected ("dirty") maps and the CLEAN maps, from which the azimuthal structure of the beam has been removed (see Fig. 1) lends support to this conclusion.

2. The cross structure is seen in the 730 μm maps generated by two independent data reduction methods. Thus it would have to be an artifact only of the actual data sampling.

3. While the cross structure *is* approximately aligned with the right ascension and declination axes, our maps were scanned in azimuth and elevation. L1551 IRS 5 passes almost through the zenith at JCMT, and the parallactic angle is almost constant over a large range of hour angle on either side of transit. The position angle of the scan direction for most of the individual maps was either 80° (rising) or 100° (setting). The DBMEM procedure was applied independently to the rising scans and to the setting scans, and yielded consistent results.

4. The cross shape is also present in spectral line observations with similar beam size (Fuller et al. 1994). These observations of $C^{17}O$ ($2 \rightarrow 1$) emission were obtained using a different observing method where the telescope was not raster scanned but rather pointed to individual positions around L1551 IRS 5.

We therefore conclude that the cross is not generated by any aspect of our observing methodology but is rather intrinsic to the circumstellar region around IRS 5.

In Figure 3, we plot the flux at each wavelength as a function of azimuth at a radius of 20″ from the source peak. The four arms of the cross in the 730 μm data appear as distinct peaks at position angles 75°, 160°, 253°, and 345° in Figure 3. The arms of the cross are almost exactly at right angles to one another, and the cross is rotated by approximately −15° in position angle from the positive right ascension axis. The peaks in the 850 μm data correlate well with the positions of the 730 μm peaks, although the contrast between peaks and minima is generally smaller. On the other hand, the 1100 μm data show only two clear peaks (at position angles 185° and 355°), which are nearly aligned with the north and south peaks in the 850 μm and 730 μm data. Peaks to the east and west are not readily apparent in the 1100 μm data.

The ratio of the average minimum value to the average peak value in the 730 μm azimuthal cut is 0.45, whereas in the 850 μm data this ratio is 0.60. The 1100 μm data show only two clear peaks, so we calculate this ratio using the positions of the 730 μm maxima and minima, and determine a value of 0.88. The contrast between "arm" and "interarm" regions is larger for the shorter wavelength observations, suggesting that the arm emission is generated by warmer dust than is the interarm emission.

The cross is also evident in the spatial distribution of the ratio between 730 μm and 1100 μm emission, even when both maps are convolved to a common beamsize of 20″. We find

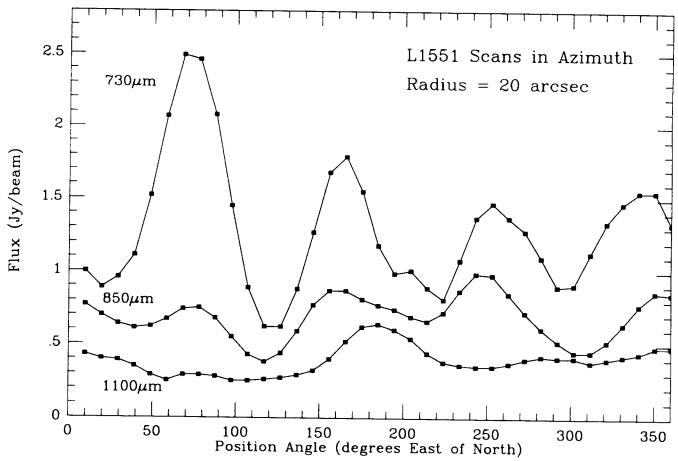


FIG. 3.—Flux as a function of azimuth at a radius of 20″ from IRS 5 at 730 μm, 850 μm, and 1100 μm, from the CLEANed NOD2 maps. The four "arms" of the cross-shaped structure in the 730 μm map appear prominently in this display.

that the position of IRS 5 is a local minimum in the ratio of 730 $\mu$m to 1100 $\mu$m emission, with a ratio of $3.3 \pm 0.1$. The ratio increases with distance from IRS 5 in all directions, but does so fastest along the eastern and western arms. At a distance of 15″ to the east and west of IRS 5, the ratio reaches $6.6 \pm 0.6$ and $5.0 \pm 0.5$, respectively. These values are significantly greater than the ratio toward IRS 5. Using the ratios at [−10″, −10″], [−10″, +10″], [+10″, +10″], and [+10″, −10″], we calculate an average off-arm ratio of 4.2 with a 1 $\sigma$ dispersion of 0.3 and a standard error in the mean of 0.2. This ratio is significantly less than the on-arm ratios listed above. The difference between the on-arm and off-arm ratios indicates that the mean temperature of the dust in the cross is higher than the mean temperature of the dust in the interarm region.

### 3.2. *Spectral Properties*

While the signal-to-noise ratio in each of the maps is very high, the uncertainty in the absolute flux calibration is still quite large, primarily because of the substantial uncertainty in the flux densities of our calibrator sources (even Mars), and variations in the atmospheric opacity which occur over timescales shorter than the time between source and calibrator observations. Based on repeated observations of the source, we estimate our 1 $\sigma$ calibration uncertainties to be 7%, 13%, and 16% for the 1100 $\mu$m, 850 $\mu$m, and 730 $\mu$m measurements, respectively. This relatively large uncertainty along with the small range in frequencies observed (less than a factor of 2) makes determination of the spectral index difficult. However, the variation in spectral shape as a function of spatial position is meaningful since calibration uncertainties will affect each map uniformly.

We calculate a spectral index $\alpha$ for the integrated map emission, assuming $F_\nu \propto \nu^\alpha$ and find a value of $4.8 \pm 0.7$. This value is consistent with optically thin, blackbody emission in the Rayleigh-Jeans limit with a dust emissivity which has a steep spectral index ($\gtrsim 2$).

The spectral index of the compact source emission is $3.3 \pm 0.8$. This spectral index is marginally smaller than the spectral index determined from the integrated fluxes, and is consistent with the spectral index ($2.4 \pm 0.5$) inferred from the 2.7 mm, 1.3 mm, and 850 $\mu$m interferometer measurements of the central source (Keene & Masson 1990; Lay et al. 1994). However, at each wavelength the flux density of our compact component is greater than the fluxes from the interferometer source. We find ratios of 0.38, 0.28, and 0.27 between the interferometer source and our compact source at 1100 $\mu$m, 850 $\mu$m, and 730 $\mu$m, respectively. The excess flux and resolved size of our compact source is likely due to the presence of additional material in an envelope around the interferometer source. The fact that the spectral index tends to increase with beam size or integration area suggests that the more compact emission is optically thick (i.e., $\alpha \sim 2$), while the more extended emission is optically thin (i.e., $\alpha \sim 4$).

Butner et al. (1991) estimate a 100 $\mu$m optical depth of 0.1 over an 11″ region and a temperature of 50 K for the material responsible for the emission seen at 50 $\mu$m and 100 $\mu$m. If we assume this temperature and extrapolate the 100 $\mu$m optical depth to submillimeter wavelengths using the emissivity law of Hildebrand (1983), we can account for ~20% of the observed submillimeter emission.

Thus, approximately half of the submillimeter emission from the compact source can be ascribed to the interferometer source (~30%) and the 50 K envelope (~20%). The remainder of the submillimeter emission must be generated such that it is not observable at 100 $\mu$m, nor with millimeter interferometers. Therefore, we conclude that approximately half of the compact source submillimeter emission is generated by cold dust distributed in an envelope around the interferometer source.

## 4. DISCUSSION

It is widely accepted that dust at a variety of temperatures can be found around forming young stars. In the section above, we have shown that both the spectral energy distribution and the spatial distribution of submillimeter emission indicate that dust at a variety of temperatures is required to replicate our data. The interesting new twist indicated by this dataset, however, is the possibility that the distribution of dust temperatures in the envelope around L1551 IRS 5 is not spherically symmetric. Below, we examine with a simple two-component model the hypothesis that the warm dust is confined to a cross-shaped structure centered on L1551 IRS 5. This model is far too simple to represent accurately the envelope structure, but it provides a means to diagnose the effects of azimuthal temperature gradients within the envelope.

### 4.1. *A Two-Component Model for the Extended Emission*

The presence of the cross emission at 730 $\mu$m and its absence at 1100 $\mu$m suggest that two spatially extended components may be contributing to the observed submillimeter emission: (1) a relatively cold, spatially extended structure whose size and orientation are shown by the 1100 $\mu$m observation; and (2) a warmer component centered on IRS 5 and having a cross-shaped spatial structure.

To test this hypothesis, we construct a simple two-component model for the submillimeter emission from L1551 IRS 5. Each component is assumed to be optically thin and characterized by a single dust temperature. We generate spatial distributions of optical depth for the cold and warm components on a 125 × 125 grid with 1″ spacing. Using the 1100 $\mu$m map as a guide, we construct the cold component optical depth as a power law in elliptical impact parameter, i.e.,

$$\tau_{\rm cold} = Aw^{-0.5} \quad \text{where} \quad w = \left[\left(\frac{x}{2}\right)^2 + \left(\frac{y}{1}\right)^2\right]^{1/2}, \qquad (1)$$

and $x$ and $y$ are impact parameters in right ascension and declination, respectively. The power-law index of −0.5 was chosen such that the volume density inferred from this column density would vary as radius to the −1.5 power, which is consistent with an "infall" density distribution (Shu 1977). We model the warm component as a "cross" 1″ in width and extending 20″ from IRS 5 to the north, south, east, and west. We assume that the dust emissivity law varies with frequency as a power law through the submillimeter range and fix its power-law index to be 2. The free parameters in this model are the temperatures and total column densities for the cold and warm components. For given input parameters, we generate maps of the flux distribution at 1100 $\mu$m and 730 $\mu$m and convolve these distributions to the beam size of our observations.

In evaluating the models, we use as our primary constraint the requirement that the cross be readily apparent in the 730 $\mu$m map and nearly invisible in the 1100 $\mu$m map (hereafter the "cross constraint"). Additionally, we require that the total integrated flux at 730 $\mu$m and 1100 $\mu$m be similar to the mea-

sured peak fluxes, after subtraction of the extrapolated interferometer source flux. These relatively simple constraints are only satisfied by a small and physically interesting set of parameters.

The "cross constraint" requires that the ratio of cold component emission to warm component emission be significantly smaller at 730 $\mu$m than at 1100 $\mu$m. This can be accomplished only if the temperature of the cold component ($T_{cold}$) is lower than the temperature of the warm component ($T_{warm}$). Furthermore, since for temperatures greater than $\sim$40 K, the entire submillimeter wavelength range is in the Rayleigh-Jeans regime and the ratio of 1100 $\mu$m to 730 $\mu$m emission is then *not* sensitive to temperature, $T_{cold}$ must be significantly less than 40 K. For the same reason, we cannot place an upper bound on $T_{warm}$. For $T_{warm} > 40$ K, changes in temperature will affect only the fitted optical depth of the warm component, and not its appearance or prominence relative to the cold component.

A series of these two-component models is compared with our data in Figure 4. We plot the distribution of 1100 $\mu$m and 730 $\mu$m emission after removing a point source whose flux is equal to the flux of the interferometer source. We assume an 1100 $\mu$m flux of 1.15 Jy and a 730 $\mu$m flux of 3.1 Jy for the inerferometer source, based on the Keene & Masson (1991) and Lay et al. (1994) fluxes and a spectral index of 2.5. For the models, we have fixed $T_{warm} = 50$ K, in light of the observed 50 $\mu$m and 100 $\mu$m color temperature. We have varied $T_{cold}$ from 8 K on the left to 20 K on the far right. The "cross constraint" is best satisfied by the models with $T_{cold} < 16$ K.

Models with $T_{cold} \geq 16$ K do not satisfy the cross constraint because the cross is not visible at 730 $\mu$m. For these models, the difference in temperature between the cold and warm components is not great enough to distinguish the 1100 $\mu$m spatial distribution from the 730 $\mu$m spatial distribution. In the extreme case ($T_{cold} = 20$ K), the two maps look nearly identical and have only the smooth structure of the cold component.

Optical depths, and hence masses, are more poorly constrained than the temperatures, first because they depend directly on the derived temperatures, second because they depend on our absolute calibration, and third because they depend on an uncertain conversion factor from submillimeter optical depth to hydrogen column density. These uncertainties notwithstanding, we can conclude from our modeling exercise that the cold component must have much higher mass than the warm component For $T_{cold} = 12$ K, we find that a cold component mass of 1.2 $M_\odot$ within the mapped area is required to produce the observed flux. This mass produces an average hydrogen column density of $3 \times 10^{22}$ cm$^{-2}$ within 15″ of IRS 5, which is consistent with results from molecular line tracers (Menten et al. 1989; Fuller et al. 1994). This cold mass is also consistent with the mass of the infalling envelope expected from theoretical calculations (Shu 1977; Adams et al. 1987). The warm component requires significantly less mass—approximately 0.02 $M_\odot$ if $T_{warm} = 50$ K. This mass of 50 K material is also sufficient to produce the 100 $\mu$m flux observed by Butner et al. (1991).

While the spatial and temperature structure of the envelope surrounding IRS 5 is undoubtedly much more complicated than the simple model presented here, we believe that several basic conclusions can be drawn from our two-component study: (1) the envelope surrounding IRS 5 must contain a substantial amount of cold dust with temperatures less than about 16 K; (2) warmer dust with temperatures greater than about 40 K must also be present and *must be distributed non-axisymmetrically*; (3) the mass of cold dust is much greater than the mass of warm dust, and the total mass is probably in

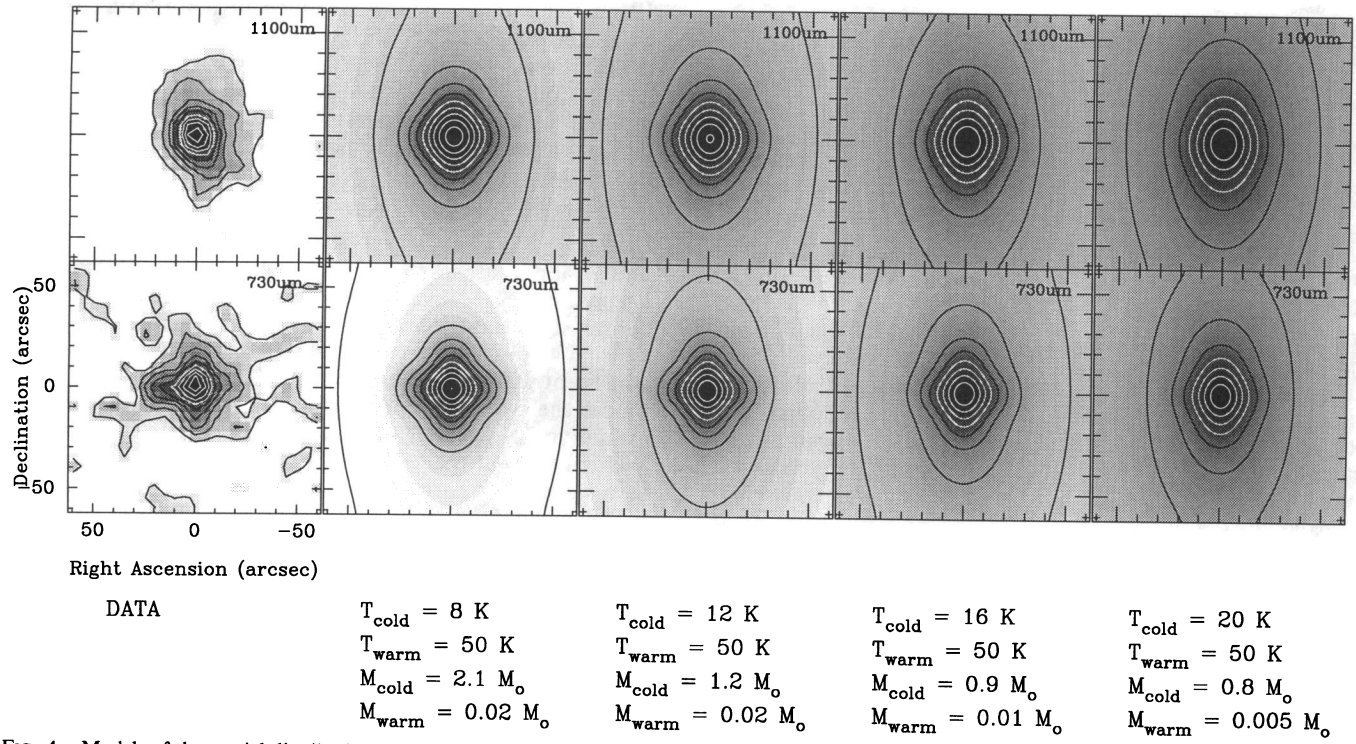


FIG. 4.—Models of the spatial distribution of 1100 $\mu$m (*top*) and 730 $\mu$m emission for the two component model discussed in the text. Point source response functions with the flux of the KM source have been subtracted from the 1100 $\mu$m and 730 $\mu$m maps at left. For all four models shown, $T_{warm} = 50$ K, while $T_{cold}$ increases from 8 K (*left*) to 20 K (*right*). All plots have 10% contours.

the range 0.6–2.0 $M_\odot$ (excluding the mass associated with the interferometer source). Detailed geometric models of the envelope surrounding IRS 5 should be constrained by these results. In particular, we note that spherically symmetric or even rotationally flattened geometries are not likely to reproduce our observations.

### 4.2. *Speculation Regarding the Origin of the Cross*

The structure of the cross, its position on the sky, and its warm dust temperature strongly indicate that it is closely associated with IRS 5. Furthermore, the orientation of the arms of the cross suggest that it has resulted from an interaction between dense circumstellar material and the outflow from IRS 5.

The CO outflow from IRS 5 has been well measured by a variety of observers (Snell, Loren, & Plambeck 1980, Snell & Schloerb 1985; Moriarty-Schieven et al. 1987; Uchida et al. 1987; Moriarty-Schieven & Snell 1988). It is a highly elongated, bipolar structure centered on IRS 5 with its long axis at a position angle of 45°. Although on large scales, the outflow is well collimated, it has a relatively large opening angle of almost 90° near IRS 5 (Moriarty-Schieven & Snell 1988). Studies of the velocity structure of the CO emission indicate that the outflow lobes consist of a central cavity containing little or no molecular material surrounded by a shell of high-velocity molecular material (Snell & Schloerb 1985; Moriarty-Schieven et al. 1987; Uchida et al. 1987).

When superposed as in Figure 5, the relationship between the cross and outflow is unmistakable. From the spatial relationship alone, it appears obvious that the material in the cross demarks the edge of the outflow cavity near IRS 5. Furthermore, the cross emission is generated by warm dust, suggesting an interaction between the outflow and cross material. Finally, Fuller et al. (1994) report that spectral line measurements of the cross material have a broader line width than spectra of material not associated with the cross, indicating a dynamic interaction between cross and outflow.

We conclude then that the interaction between the outflow from IRS 5 and its surrounding dense core has produced the cross structure that we see at 850 $\mu$m and 730 $\mu$m. While we cannot determine from these data whether the cross material is responsible for confining the outflow, we note that the mass contained within the cross is probably a very small fraction of the total mass surrounding IRS 5, and that the cross has an opening angle of nearly 90°, while the outflow on larger scales is confined to smaller angles, and suggest that the cross may be material pushed aside by the energetically dominant outflow.

## 5. CONCLUSIONS

1. We present high signal-to-noise ratio submillimeter continuum maps of the dust distribution around L1551 IRS 5. The maps are dominated by a compact source at the position of IRS 5, whose size is slightly larger than the beamsize of our observations. Gaussian deconvolution of the beam from the compact source distribution indicates a compact source size of about 10″ (~1400 A.U.).

2. Low-level emission extending up to 30″ from IRS 5 is observed in all three submillimeter continuum maps. The emission has azimuthal structure, indicating that the dust distribution around IRS 5 is not spherically symmetric. The 1100 $\mu$m emission is extended in the north-south direction, while the 850 $\mu$m and 730$\mu$m maps show a crosslike structure with extensions to the north, south, east, and west.

3. A simple two-component model can explain in general terms the spatial distribution of extended emission in all three maps. The model comprises a relatively massive (~1 $M_\odot$) cold (~12 K) component and a much less massive ($\lesssim$0.02 $M_\odot$) warmer ($\gtrsim$50 K) component. The spatial distribution of the

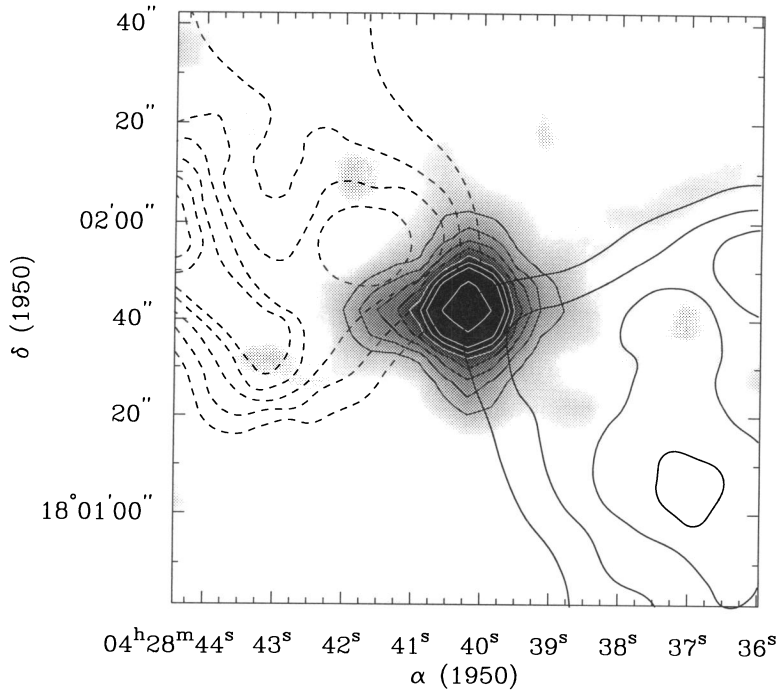


FIG. 5.—Gray scale and contours of the 730 $\mu$m emission overlain with contours of red- and blueshifted CO emission from Moriarty-Schieven & Snell (1988). The 730 $\mu$m contours increment from 10% to 90% of peak flux by 10%. The redshifted CO emission (*dashed contours*) is integrated over a 8–23 km s$^{-1}$ velocity range and the blueshifted CO emission (*solid contours*) is integrated over a −9 to 5 km s$^{-1}$ range.

cold component is similar to the distribution of 1100 $\mu$m extended emission, while the warm component is confined to a cross centered on IRS 5 and extending 20″ to the north, south, east, and west.

4. The cold component can be interpreted as the envelope surrounding IRS 5, out of which material may be accreting onto the central source. The structure and orientation of the cross-shaped warm component indicate that the cross is closely associated with the outflow from IRS 5. We suggest that the edges of the cavity excavated by the outflow as it passes through the dense core are warmed either radiatively or dynamically and are observed as the cross emission seen at 850 $\mu$m and 730 $\mu$m.

The authors thank the telescope operators and support staff of the JCMT for their assistance in the data acquisition. E. F. L. acknowledges the support of the James Clerk Maxwell Telescope Fellowship while in residence at the Institute for Astronomy at the University of Hawaii. G. A. F. acknowledges the support of a NRAO Jansky Fellowship and the Origins of the Solar System Program.

## REFERENCES

Adams, F. C., Lada, C. J., & Shu, F. H. 1987, ApJ, 312, 788
Benson, P. J., & Myers, P. C. 1989, ApJS, 71, 89
Butner, H. M., Evans, N. J., Lester, D. F., Levreault, R. M., & Strom, S. E. 1991, ApJ, 376, 636
Campbell, B., Persson, S. E., Strom, S. E., & Grasdalen, G. L. 1988, AJ, 95, 1173
Cohen, M., Harvey, P. M., Schwartz, R. D., & Wilking, B. A. 1984, ApJ, 278, 671
Elias, J. 1978, ApJ, 224, 857
Fuller, G. A., Ladd, E. F., Padman, R., Adams, F. C., & Myers, P. C. 1994, ApJ, submitted
Gull, S. F., & Skilling, J. 1989, The MEMSYS3 User's Manual, Maximum Entropy Data Consultants, Ltd.
Hildebrand, R. H. 1983, QJRAS, 24, 267
Hodapp, K.-W., Capps, R., Strom, S. E., Salas, L., & Grasdalen, G. L. 1988, ApJ, 335, 814
Hogböm, J. A. 1974, A&AS, 15, 417
Keene, J., & Masson, C. R. 1990, ApJ, 355, 635
Lay, O. P., Carlstrom, J. E., Hills, R. E., & Phillips, T. G. 1994, ApJ, 434, L75
Menten, K. M., Harju, J., Olano, C. A., & Walmsley, C. M. 1989, A&A, 223, 258
Moriarty-Schieven, G. H., & Snell, R. L. 1988, ApJ, 332, 364
Moriarty-Schieven, G. H., Snell, R. L., Strom, S. E., Schloerb, F. P., Strom, K. M., & Grasdalen, G. L. 1987, ApJ, 319, 742
Myers, P. C., Fuller, G. A., Goodman, A. A., & Benson, P. J. 1991, ApJ, 376, 561
Richer, J. S. 1992, MNRAS, 254, 165
Sargent, A. I., Beckwith, S., Keene, J., & Masson, C. R. 1988, ApJ, 333, 936
Shu, F. H. 1977, ApJ, 214, 488
Snell, R. L., Loren, R. B., & Plambeck, R. L. 1980, ApJ, 239, L17
Snell, R. L., & Schloerb, F. P. 1985, ApJ, 295, 490
Strom, K. M., Strom, S. E., & Vrba, F. J. 1976, AJ, 81, 320
Strom, S. E., Strom, K. M., Grasdalen, G. L., Capps, R. W., & Thompson, D. 1985, AJ, 90, 2575
Uchida, Y., Kaifu, N., Shibata, K., Hayashi, S. S., & Hasegawa, T. 1987, in IAU Symp. 115, Star Forming Regions, ed. M. Peimbert & J. Jugku (Dordrecht: Reidel), 287
Walker, C. K., Adams, F. C., & Lada, C. J. 1990, ApJ, 349, 515